RESEARCH PAPER

PCCP
www.rsc.org/pccp

Untangling the formation of the cyclic carbon trioxide isomer in low temperature carbon dioxide ices

Chris J. Bennett,[a] C. Jamieson,[a] Alexander M. Mebel[b] and Ralf I. Kaiser*[ac]

[a] *Department of Chemistry, University of Hawai'i at Manoa, Honolulu HI 96822, USA. E-mail: kaiser@gold.chem.hawaii.edu*
[b] *Department of Chemistry and Biochemistry, Florida International University, Miami FL 33199, USA*
[c] *Department of Physics & Astronomy, The Open University, Milton Keynes, UK MK7 6AA*

Received 1st December 2003, Accepted 12th January 2004
First published as an Advance Article on the web 23rd January 2004

The formation of the cyclic carbon trioxide isomer, $CO_3(X\ ^1A_1)$, in carbon-dioxide-rich extraterrestrial ices and in the atmospheres of Earth and Mars were investigated experimentally and theoretically. Carbon dioxide ices were deposited at 10 K onto a silver (111) single crystal and irradiated with 5 keV electrons. Upon completion of the electron bombardment, the samples were kept at 10 K and were then annealed to 293 K to release the reactants and newly formed molecules into the gas phase. The experiment was monitored *via* a Fourier transform infrared spectrometer in absorption-reflection-absorption (solid state) and through a quadruple mass spectrometer (gas phase) on-line and *in situ*. Our investigations indicate that the interaction of an electron with a carbon dioxide molecule is dictated by a carbon–oxygen bond cleavage to form electronically excited (^{1}D) and/or ground state (^{3}P) oxygen atoms plus a carbon monoxide molecule. About 2% of the oxygen atoms react with carbon dioxide molecules to form the C_{2v} symmetric, cyclic CO_3 structure *via* addition to the carbon–oxygen double bond of the carbon dioxide species; neither the C_s nor the D_{3h} symmetric isomers of carbon trioxide were detected. Since the addition of O(^{1}D) involves a barrier of a 4–8 kJ mol^{-1} and the reaction of O(^{3}P) with carbon dioxide to form the carbon trioxide molecule *via* triplet-singlet intersystem crossing is endoergic by 2 kJ mol^{-1}, the oxygen reactant(s) must have excess kinetic energy (suprathermal oxygen atoms which are not in thermal equilibrium with the surrounding 10 K matrix). A second reaction pathway of the oxygen atoms involves the formation of ozone *via* molecular oxygen. After the irradiation, the carbon dioxide matrix still stores ground state oxygen atoms; these species diffuse even at 10 K and form additional ozone molecules. Summarized, our investigations show that the cyclic carbon trioxide isomer, $CO_3(X\ ^1A_1)$, can be formed in low temperature carbon dioxide matrix *via* addition of suprathermal oxygen atoms to carbon dioxide. In the solid state, $CO_3(X\ ^1A_1)$ is being stabilized by phonon interactions. In the gas phase, however, the initially formed C_{2v} structure is rovibrationally excited and can ring-open to the D_{3h} isomer which in turn rearranges back to the C_{2v} structure and then loses an oxygen atom to 'recycle' carbon dioxide. This process might be of fundamental importance to account for an ^{18}O enrichment in carbon dioxide in the atmospheres of Earth and Mars.

1 Introduction

Ever since the first tentative characterization of the carbon trioxide molecule in photolyzed ozone–carbon dioxide ices at 77 K,[1] the CO_3 species has been a subject of various spectroscopic and theoretical studies. Moll *et al.*[1] and Jacox *et al.*[2] assigned four fundamentals at 2045 cm^{-1} (C=O stretch), 1073 cm^{-1} (O–O stretch), 972 cm^{-1} (C–O stretch), 593 cm^{-1} (C–O stretch), and 568 cm^{-1} (O–C=O stretch) in low temperature carbon dioxide matrices; in argon matrices, these absorptions were shifted to 2053 cm^{-1}, 1070 cm^{-1}, 975 cm^{-1}, and 564 cm^{-1};[3] no feature around 593 cm^{-1} was identified in solid argon. Absorptions at 1894 cm^{-1} (argon matrix) and 1880 cm^{-1} (carbon dioxide matrix) were tentatively assigned as a Fermi resonance of the 2045 cm^{-1} band with an overtone of the 972 cm^{-1} fundamental. Jacox *et al.* conducted also a normal coordinate analysis and suggested a C_{2v} bridged structure (Fig. 1(1)); in strong contrast, LaBonville *et al.* allocated a C_s symmetric structure of the carbon trioxide molecule (Fig. 1(2)).[4]

The interest in the carbon trioxide molecule has been also fueled by the complex reaction mechanisms of carbon oxides (carbon monoxide and carbon dioxide) with atomic oxygen in the Martian atmosphere.[5–8] Carbon dioxide, $CO_2(X\ ^1\Sigma_g^+)$, presents the major constituent (95.3% by volume); nitrogen (2.7%), argon (1.6%), carbon monoxide (0.7%), molecular oxygen (0.13%), water (150–200 ppm), and ozone (0.03 ppm) make up the rest.[9] It has been suggested that the photodissciation of carbon dioxide by solar photons ($\lambda < 2050$ Å) produces carbon monoxide and atomic oxygen. Near the threshold, only ground state O(^{3}P) atoms are produced; shorter wavelengths supply also O(^{1}D).[5] The primary fate of electronically excited oxygen atoms is thought to be quenching to form O(^{3}P); the

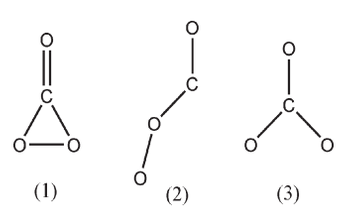

Fig. 1 Proposed structures of carbon trioxide isomers.

DOI: 10.1039/b315626p

detailed process is not known and has been postulated to proceed *via* a carbon trioxide molecule. Once $O(^3P)$ and carbon monoxide has been formed, it is difficult to restore carbon dioxide, since the reversed reaction is spin forbidden. Detailed photochemical models suggest that the oxygen atoms rather react to molecular oxygen and ultimately to ozone.[5]

The CO_3 molecule has been also implied as an important intermediate in the ^{18}O isotope enrichment of carbon dioxide in the atmospheres of Earth and Mars.[10,11] Computations and laboratory experiments indicate that the ^{18}O enrichment in ozone might be transferable to carbon dioxide,[12,13] possibly *via* a CO_3 intermediate. On Earth, photolysis of stratospheric ozone generates $O(^1D)$, which in turn might react with carbon dioxide to form a carbon trioxide molecule. In the gas phase, the latter was postulated to fragment to carbon dioxide and atomic oxygen, possibly inducing an isotopic enrichment in carbon dioxide *via* isotopic scrambling.[14] However, the explicit structure of the CO_3 intermediate has not been unraveled yet.

Various kinetic measurements have been carried out to determine the temperature-dependent rate constants of the reaction of electronically excited oxygen atoms, $O(^1D)$, with carbon dioxide. At room temperature, rate constants of a few 10^{-10} cm^3 s^{-1} have been derived.[15–17] This order of magnitude suggest that the reaction has no or only little activation energy, proceeds with almost unit efficiency, and most likely involves a reaction intermediate. However, neither reaction products nor the nature of the intermediate were determined. On the other hand, a $CO(X\ ^1\Sigma^+) + O_2(X\ ^3\Sigma_g^-)$ exit channel was found to have an activation energy between 15 and 28 kJ mol^{-1} in the range of 300–2500 K.[18] This finding correlates also with a theoretical investigation of the singlet and triplet potential energy surfaces of the CO_3 system.[19] Froese and Goddard suggested that the barrier-less, spin-forbidden quenching pathway to form ground state oxygen atoms and carbon dioxide ($\Delta_R G = -190.0$ kJ mol^{-1}) dominates over the formation of $CO(X\ ^1\Sigma^+)$ plus $O_2(X\ ^3\Sigma_g^-)$ ($\Delta_R G = -157.5$ kJ mol^{-1}) and $CO(X\ ^1\Sigma^+)$ plus $O_2(a\ ^1\Delta_g)$ ($\Delta_R G = -63.3$ kJ mol^{-1}). Further theoretical calculations indicated that the CO_3 isomer identified in the carbon dioxide and argon matrices might be the C_{2v} symmetric bridged molecule. A D_{3h} structure was identified as a local minimum, too, but lies 16.8 kJ mol^{-1} higher in energy than the cyclic isomer (Fig. 1, (3)); according to calculations, both structures are connected *via* a transition state located 36 kJ mol^{-1} above the cyclic molecule.[20] At temperatures higher than 100 K, the cyclic CO_3 isomer was predicted to decay to carbon dioxide and ground state oxygen atoms *via* singlet-triplet transitions.

Despite this information on the reaction of carbon dioxide with atomic oxygen, an incorporation of these data into homogeneous gas phase models still fails to reproduce the observed abundances of carbon dioxide, carbon monoxide, oxygen, and ozone in the Martian atmosphere quantitatively.[9] Atreya *et al.* pointed out the necessity to include heterogeneous reactions on aerosols or carbon dioxide ice particles in the Martian air.[21–23] However, these processes have not been investigated in the laboratory so far. Also, the explicit structure and the actual formation mechanism of the CO_3 isomer and its role in the ^{18}O isotopic enrichment in stratospheric carbon dioxide remain to be solved.

In this paper, we present a detailed experimental and theoretical investigation on the formation mechanism of carbon trioxide in low temperature carbon dioxide ices and the implications for gas phase chemistry. Reactive oxygen atoms are generated *via* electronic energy loss of high energy electrons to the carbon dioxide molecule in the solid sample. Our first goal is to identify the infrared absorption features of the carbon trioxide molecule, to resolve the true nature of the 1880 cm^{-1} absorption of the carbon trioxide molecule unambiguously, and to assign the structure of the newly formed species. Secondly, reaction mechanisms to synthesize the carbon trioxide molecule together with other newly formed species will be derived combining our experimental data with electronic structure calculations. Finally, important implications of these results to planetary and atmospheric chemistry are addressed. Note that these studies also have important implications to planetary, cometary, and interstellar chemistry since carbon dioxide has been identified as a major component of ices on Mars, in comets such as Halley,[24] and of low temperature grain mantles in cold molecular clouds like the Taurus Molecular Cloud (TMC-1).[25]

2 Theoretical calculations

The geometries of various local minima and transition states on three potential energy surfaces (PESs) of carbon trioxide, CO_3, including the lowest triplet and two lowest singlet electronic states, have been optimized using the multireference complete active space self-consistent field (CASSCF) method[26,27] with the 6-311G(d) basis set. The active space in the CASSCF calculations included 16 electrons distributed over 13 orbitals, *i.e.*, this was the full-valence active space excluding 2s lone pairs on three oxygen atoms. Vibrational frequencies and infrared (IR) intensities have been also computed at the CASSCF(16,13)/6-311G(d) level of theory. Single-point energies for various species have been subsequently refined employing internally-contracted multireference configuration interaction MRCI method[28,29] with the same (16,13) active space and the larger 6-311+G(3df) basis set. All calculations were carried out using the MOLPRO 2002[30] and DALTON[31] programs.

3 Experimental

The experiments were carried out in a contamination-free ultrahigh vacuum (UHV) chamber; the top view of this machine is shown in Fig. 2. This setup consists of a 15 l cylindrical stainless steel chamber of 250 mm diameter and 300 mm height which can be evacuated down to 2×10^{-10} torr by a magnetically suspended turbopump backed by an oil-free scroll pump. A two stage closed cycle helium refrigerator-interfaced to a differentially pumped rotary feedthrough is attached to the lid of the machine and holds a polished silver (111) single crystal. This crystal is cooled to 10.4 ± 0.3 K, serves as a substrate for the ice condensate, and conducts the heat generated from the impinging electrons to the cold head.

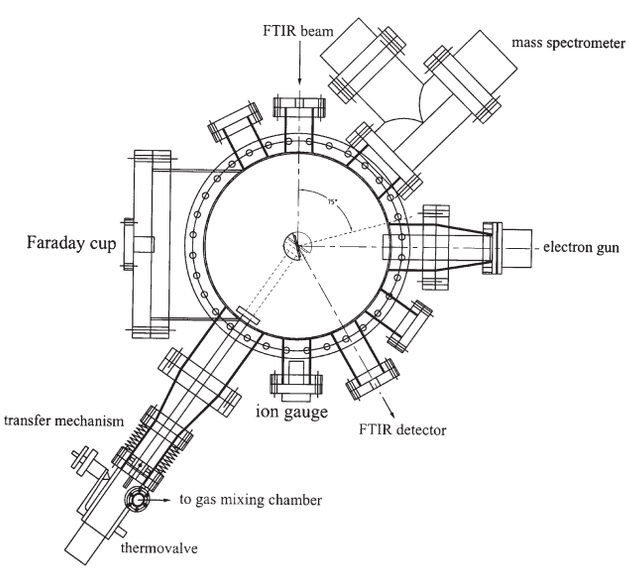

Fig. 2 Top view of the experimental setup.

This journal is © The Owner Societies 2004

To minimize the radiative heat transfer from the chamber walls to the target, a 40 K aluminum radiation shield is connected to the second stage of the cold head and surrounds the crystal. The ice condensation is assisted by a precision leak valve. During the actual gas condensation, the deposition system can be moved 5 mm in front of the silver target. This setup guarantees a reproducible thickness and composition of the frosts. To allow a selection of the target temperature, a temperature sensor, cartridge heater, and a programmable controller are interfaced to the target.

The carbon dioxide ices were prepared at 10 K by depositing carbon dioxide gas onto the cooled silver crystal. Blank checks of the pure gas (BOC Gases, 99.999%) *via* a quadrupole mass spectrometer and of the frosts *via* a Fourier transform infrared spectrometer were also carried out. Fig. 3 depicts a typical infrared spectrum of the frost; the absorptions are compiled in Table 1. To determine the ice composition quantitatively, we integrated numerous absorption features and calculated the column density, *i.e.* the numbers of absorbing molecules per cm^2, *n*, *via* the Lambert–Beer relationship (1) and eqns. (2)–(3). The integrated absorption features, the corresponding integral absorption coefficients, and the column densities are summarized in Table 2. These data suggest a column density of $(1.1 \pm 0.3) \times 10^{18}$ molecules cm^{-2}. Considering a density of 1.7 g cm^{-3} at 10 K,[32] this translates into an averaged target thickness of 0.48 ± 0.11 μm. We would like to stress that the integrated absorption coefficients have been taken in transmission experiments,[47] but the experiment has been carried out in an absorption–reflection–absorption mode. This probably causes the large variations in the film thicknesses estimated from different absorption features.

$$I(\tilde{\nu}) = I_0(\tilde{\nu})e^{-\varepsilon(\tilde{\nu})n} \quad (1)$$

with the intensity of the IR beam after, $I(\tilde{\nu})$, and before absorption, $I_0(\tilde{\nu})$, at a wavenumber $\tilde{\nu}$, the wavenumber dependent absorption coefficient $\varepsilon(\tilde{\nu})$ in units of cm^{-2} and the number of absorbing species per cm^2, *n*. Reformulating eqn. (1) with $A(\tilde{\nu}) = \lg(I_0(\tilde{\nu})/I(\tilde{\nu}))$ gives

$$A(\tilde{\nu}) = \varepsilon(\tilde{\nu})n/\ln 10. \quad (2)$$

Integrating from $\tilde{\nu}_1$ to $\tilde{\nu}_2$ yields

$$n = \frac{\ln 10 \int_{\tilde{\nu}_1}^{\tilde{\nu}_2} A(\tilde{\nu})d\tilde{\nu}}{A_{exp}} \frac{\cos(75°)}{2} \quad (3)$$

with the integrated absorption $\int_{\tilde{\nu}_1}^{\tilde{\nu}_2} A(\tilde{\nu})d\tilde{\nu}$ in cm^{-1} and the integral absorption coefficient $A_{exp} = \int_{\tilde{\nu}_1}^{\tilde{\nu}_2} \varepsilon(\tilde{\nu})d\tilde{\nu}$ in cm. The factor cos(75°) accounts for angle between the surface normal of the silver wafer and the infrared beam, whereas the division by two corrects for the ingoing and outgoing IR beams.

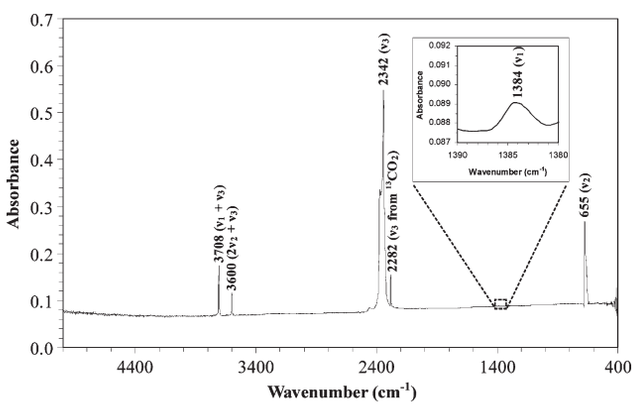

Fig. 3 Infrared spectrum of the carbon dioxide frost at 10 K. The assignments of the peaks are compiled in Table 1.

Table 1 Infrared absorptions of the carbon dioxide frosts and assignment of the observed bands according to ref. 46

Frequency/cm^{-1}	Assignment	Characterization
3708	$\nu_1 + \nu_3$	Combination
3600	$2\nu_2 + \nu_3$	Combination
2342	ν_3	Asymmetric stretch
2282	ν_3 ($^{13}CO_2$)	Isotope peak
1384	ν_1	Symmetric stretch
658, 654	ν_2	In plane/out of plane bending
638	ν_2 ($^{13}CO_2$)	Isotope peak

These ices were irradiated isothermally at 10 K with electrons of 5 keV kinetic energy generated in an electron gun at beam currents of 100 nA (60 min) by scanning the electron beam over an area of 3.0 ± 0.4 cm^2. Accounting for the extraction efficiency of 78.8% and the irradiation time, this exposes the target to 1.77×10^{15} electrons. Higher beam currents, which increase the temperature of the frost surface, should be avoided. After the actual irradiation, the sample was kept isothermally at 10 K and heated then by 0.5 K min^{-1} to 293 K.

To guarantee an identification of the reaction products in the ices and those subliming into the gas phase on line and *in situ*, two detection schemes are incorporated: (*i*) a Fourier transform infrared spectrometer (FTIR), and (*ii*) a quadrupole mass spectrometer (QMS). The chemical modification of the ice targets is monitored during the experiments to extract time-dependent concentration profiles and hence production rates of newly formed molecules and radicals in the solid state. The latter is sampled *via* a Nicolet 510 DX FTIR spectrometer (6000–500 cm^{-1}) operating in an absorption–reflection–absorption mode (reflection angle $\alpha = 75°$; Fig. 2); spectra were accumulated for 2.5 min at a resolution of 2 cm^{-1}. The infrared beam is coupled *via* a mirror flipper outside the spectrometer, passes through a differentially pumped potassium bromide (KBr) window, is attenuated in the ice sample prior and after reflection at a polished silver waver, and exits the main chamber through a second differentially pumped KBr window before being monitored *via* a liquid nitrogen cooled detector (MCTB). The gas phase is monitored by a quadrupole mass spectrometer (Balzer QMG 420) with electron impact ionization at 90 eV electron energy of the neutral molecules in the residual gas analyzer mode. The raw data, *i.e.* the temporal development of the ion currents of distinct mass-to-charge ratios, are processed *via* matrix interval algebra to compute absolute partial pressures of the gas phase molecules.[33] Since, for example, carbon dioxide can fragment to molecular oxygen and also to carbon monoxide in the ionizer of the quadrupole mass spectrometer, different molecular species add to one mass to charge ratio (*m*/*z*) of, *e.g.* 32 (O_2). Therefore, we must perform the raw data processing *via* matrix interval algebra to calculate the actual partial pressures of the

Table 2 Integral absorption coefficients A_{exp} of three absorptions of solid carbon dioxide, the integrated peak area of the absorptions in our experiments, the calculated column densities *n*, and the target thickness of the carbon dioxide sample, *d*; the integral absorption coefficients were taken from ref. 47

Peak/ cm^{-1}	Peak area/ cm^{-1}	A_{exp}/ cm $molecule^{-1}$	*n*/ molecule cm^{-2}	*d*/ μm
3745–3670	4.629	1.4×10^{-18}	9.9×10^{17}	0.42
3624–3574	2.266	4.5×10^{-19}	1.5×10^{18}	0.64
2288–2261	2.601	7.8×10^{-17}	9.0×10^{17}*	0.38[a]

[a] ^{13}C peak; values were multiplied by 100/1.1 to account for the 1.1% abundance of ^{13}C.

molecules in the gas phase. Briefly, m/z ratios are chosen to result in an inhomogeneous system of linear equations including the measured ion current (right hand vector), partial pressures (unknown quantity), and calibration factors of fragments of individual gaseous species determined in separate experiments. Since all quantities are provided with experimental errors, matrix interval arithmetic, *i.e.* an IBM high accuracy arithmetic subroutine defining experimental uncertainties as intervals, is incorporated in the computations to extract individual, calibrated components of gas mixtures.

4 Results

4.1 Computational results

Our calculations suggest that two minima exist on the lowest singlet CO_3 potential energy surface (PES): a C_{2v}-symmetric three-member cyclic structure **s1** and a D_{3h}-symmetric isomer **s2** (Fig. 4). **s1** and **s2** have similar energies and reside 197.5 and 197.1 kJ mol^{-1} lower than the $O(^1D)+CO_2(X\ ^1\Sigma_g^+)$ asymptote, respectively. These two singlet isomers can rearrange to each other by ring opening/ring closure and are separated by a low barrier of 18.4 kJ mol^{-1} with respect to **s1** occurring at transition state **s-TS1**. The cyclic structure **s1** can be produced in a reaction between $O(^1D)$ and $CO_2(X\ ^1\Sigma_g^+)$. The calculations suggest that the reactants first form a weakly bound complex ($\sim$2.9 kJ mol^{-1}) **s5**, which then rearranges to **s1** with a barrier *via* **s-TS2** of 5.6–7.6 kJ mol^{-1} relative to $O(^1D)+CO_2$. In the triplet electronic state, separated $O(^3P)$ and CO_2 have the lowest energy, while the C_{2v} isomer **t1** ($^3B_2$) resides 96.3 kJ mol^{-1} higher. **t1** has a structure rather similar to that of **s2**, except that the three C–O bond lengths are not equal; there are one double (1.201 Å) and two single (1.343 Å) bonds. Isomer **t1** can decompose to $O(^3P)+CO_2$ overcoming a barrier 51.5 kJ mol^{-1} at transition state **t-TS1**. In the reverse direction, the barrier for the $O(^3P)+CO_2(X\ ^1\Sigma_g^+)\rightarrow$ **t1** reaction is calculated to be as high as 147.7 kJ mol^{-1}. Interestingly, we were able to locate a minimal energy crossing point (MSX) between the lowest triplet and singlet electronic states in a close vicinity of **t-TS1**, both the geometry and energy of MSX are similar to those for the triplet transition state. Another possible isomer of triplet CO_3, C_s-symmetric OCOO **t2** ($^3A''$) is much less favorable and lies 260.7 kJ mol^{-1} higher in energy than $O(^3P)+CO_2(X\ ^1\Sigma_g^+)$. In addition, we found two local minima on PES of the first excited singlet electronic state, which have lower energies than $O(^1D)+CO_2(X\ ^1\Sigma_g^+)$. For instance, **s3** ($C_{2v}$, $^1A_2$) is a complex of $O(^1D)$ with carbon dioxide and stabilized by 27.6 kJ mol^{-1} relative to the separated species. The structure of **s4** (C_s, $^1A''$) is similar to that of **s2**, however, all three C–O bonds and OCO angles are slightly unequal. Transition state **s-TS2** separating **s3** and **s4** lies 46.4 and 159.8 kJ mol^{-1} above $O(^1D)+CO_2(X\ ^1\Sigma_g^+)$ and **s4**, respectively. Table 3 summarizes the infrared absorptions of **s1**, **s2**, and **t2**.

4.2 Infrared spectroscopy

The FTIR spectra are analyzed in three steps. First, we investigate the new absorptions qualitatively and assign their carriers. Hereafter, the temporal developments of these absorptions upon electron irradiation are investigated quantitatively as outlined in Section 3. Finally, these data are fitted to calculate production rates of synthesized molecules in units of molecules cm^{-2} (column density), molecules per impinging electron, and absorbed electron volt (eV) per target molecule (dose). The integration routine of the absorption features is accurate to $\pm$10%.[34]

4.2.1 Qualitative analysis. The effects of the electron irradiation of the carbon dioxide target are displayed in

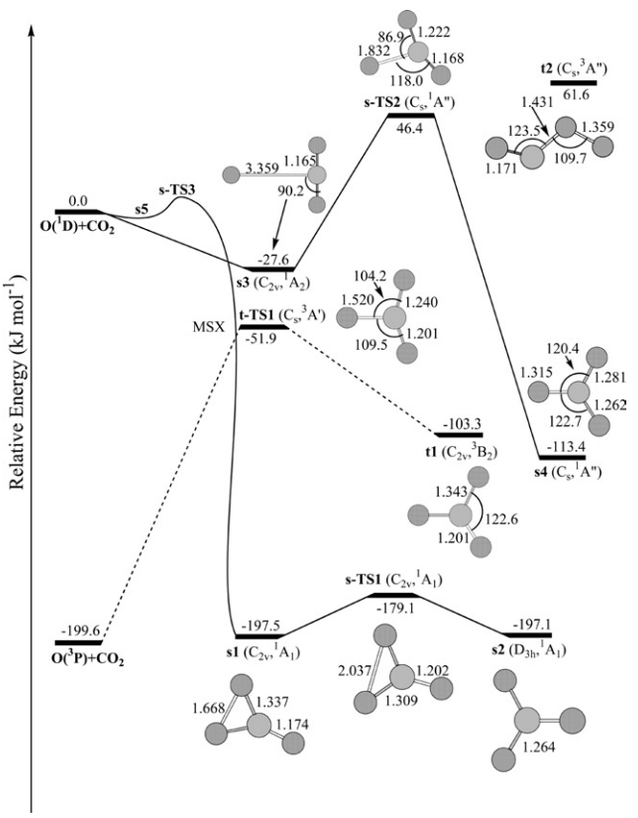

Fig. 4 Optimized geometries of various intermediates and transition states and their relative energies (in kJ mol^{-1} with zero point energy correction) obtained at the MRCI+Q(16,13) level including Davidson corrections for quadruple excitations.

Table 3 Calculated harmonic infrared absorptions frequencies of the C_{2v} (top), D_{3h} (center), and C_s (bottom) isomers of carbon trioxide isomers, the symmetry, and intensities; listed frequencies were also scaled by a factor of 0.98 to account for the anharmonicity

Mode	Symmetry	Unscaled frequency/cm^{-1}	Scaled frequency/cm^{-1}	Intensity/ cm molecule^{-1}
1	a_1	2082.9	2041	8.9×10^{-17}
2	a_1	1071.2	1050	3.8×10^{-18}
3	a_1	516.4	506	1.2×10^{-18}
4	a_1	685.1	671	6.5×10^{-18}
5	b_2	1029.4	1009	1.3×10^{-17}
6	b_2	586.3	575	1.3×10^{-18}

Mode	Symmetry	Unscaled frequency/cm^{-1}	Scaled frequency/cm^{-1}	Intensity/ cm molecule^{-1}
1	a_1	1204.0	1180	6.0×10^{-18}
2	a_1	1089.4	1067	0
3	a_1	447.5	439	1.9×10^{-19}
4	b_1	763.2	748	5.2×10^{-18}
5	b_2	1204.1	1180	6.0×10^{-17}
6	b_2	447.5	439	1.9×10^{-19}

Mode	Symmetry	Unscaled frequency/cm^{-1}	Scaled frequency/cm^{-1}	Intensity/ cm molecule^{-1}
1	a′	1931.1	1893	2.9×10^{-17}
2	a′	1026.3	1006	3.4×10^{-18}
3	a′	842.8	826	2.5×10^{-17}
4	a′	541.7	531	1.8×10^{-18}
5	a′	374.3	367	9.7×10^{-19}
6	a″	199.9	196	4.6×10^{-19}

This journal is © The Owner Societies 2004

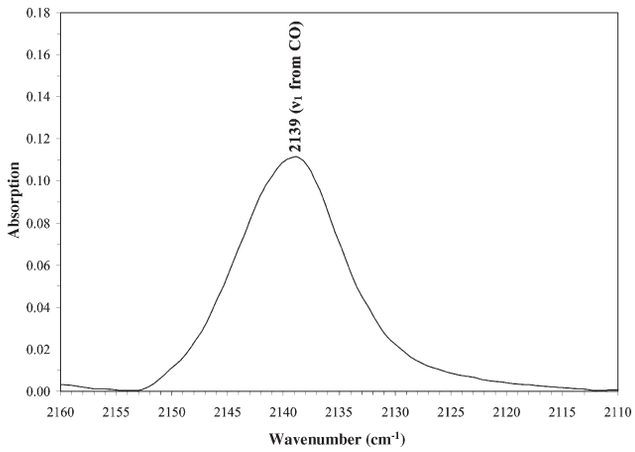

Fig. 5 Carbon monoxide absorption band (2139 cm^{-1}) as seen after a 60 min irradiation of the carbon dioxide sample at 10 K with 0.1 μA beam current.

Figs. 5–11. A comparison of the pristine sample (Fig. 3) with the irradiated ice at 10 K clearly shows new absorption features of carbon monoxide at 2139 cm^{-1} (ν_1(CO stretching); Fig. 5; Table 4)) and the corresponding isotopic pattern of ^{13}CO at 2092 cm^{-1}. These data are in close agreement to matrix isolation studies of the carbon monoxide molecule.[35]

We were also able to detect four fundamentals of the C_{2v} symmetric, cyclic CO_3 structure at 2045 cm^{-1} (ν_1), 1068 cm^{-1} (ν_2), 973 cm^{-1} (ν_5), and 565 cm^{-1} (ν_6) (Fig. 6). The position of all peaks is in excellent agreement with earlier matrix isolation studies (Section 1) and with our calculated, scaled frequencies (Table 3). Note that although the unobserved ν_3 and ν_4 modes have larger absorption coefficients than the detected ν_6 transition, the ν_4 absorption overlaps with the broad ν_2 band of the carbon dioxide reactant; the ν_3 band of carbon trioxide is too close to the cut-off of the MCTB detector to be observable. Finally, we detected also a transition at 1879 cm^{-1}, which was assigned tentatively as a Fermi resonance of the 2044 cm^{-1} band with an overtone of the 973 cm^{-1} fundamental. The calculated symmetry of the carbon trioxide

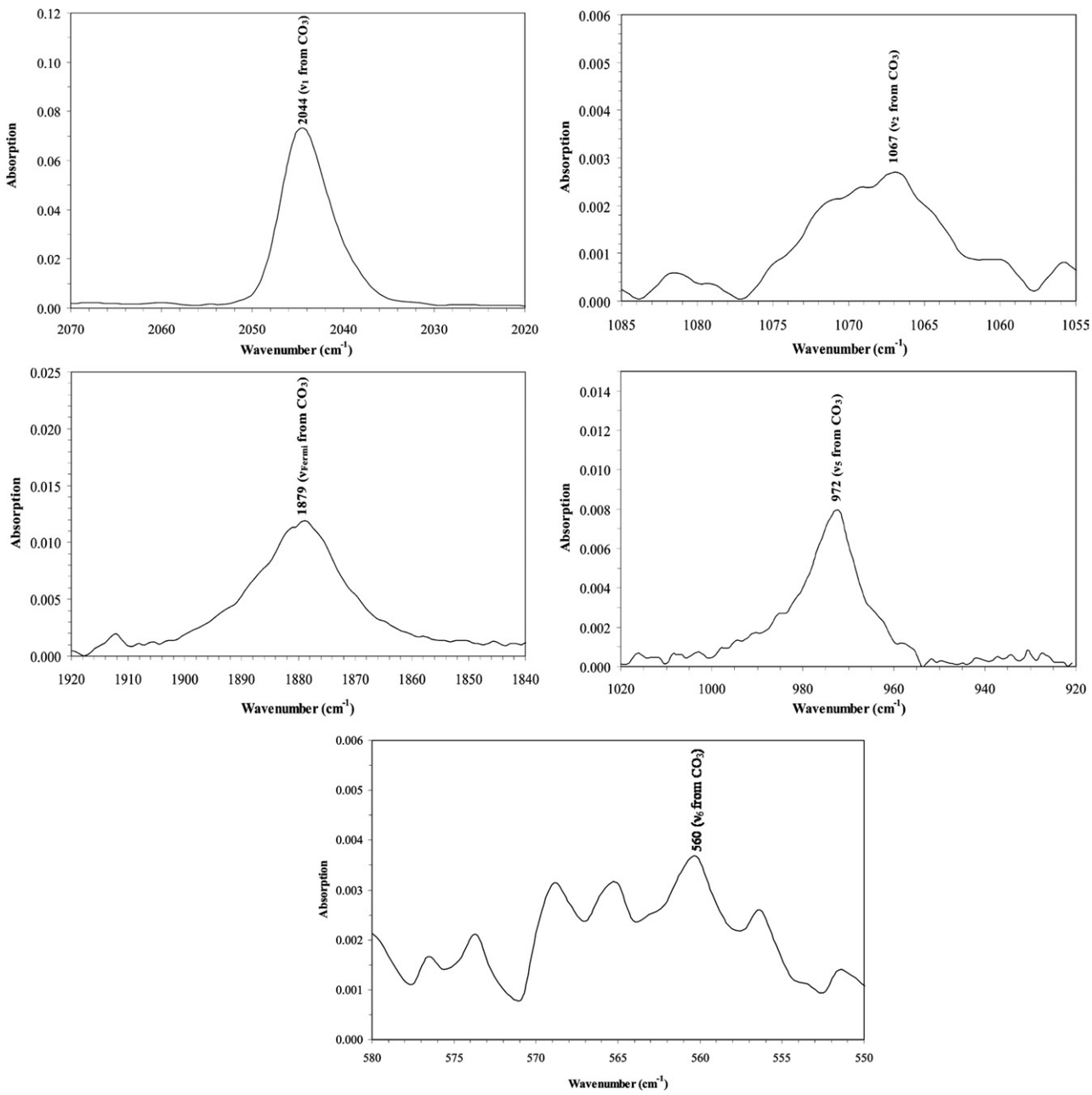

Fig. 6 Carbon trioxide absorption bands at 2044 cm^{-1}, 1879 cm^{-1}, 1067 cm^{-1}, 972 cm^{-1}, and 560 cm^{-1} as seen after a 60 min irradiation of the carbon dioxide sample at 10 K with 0.1 μA beam current.

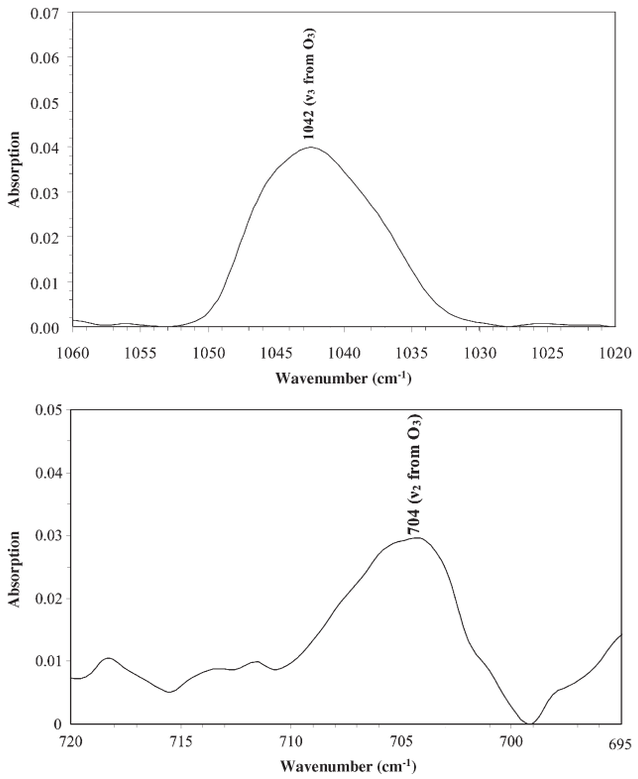

Fig. 7 Ozone absorption bands at 1042 cm^{-1} and 704 cm^{-1} as seen after a 60 min irradiation of the carbon dioxide sample at 10 K with 0.1 μA beam current.

modes (Table 3) confirm this tentative assignment. Since the ν_5 at 973 cm^{-1} has b_1 symmetry, the overtone ($2\nu_5$) holds an a_1 symmetry ($b_1 \otimes b_1 = a_1$), the latter has the same symmetry as the ν_1 fundamental; this can give rise to the Fermi resonance as observed at 1879 cm^{-1}. These data make it exceptionally

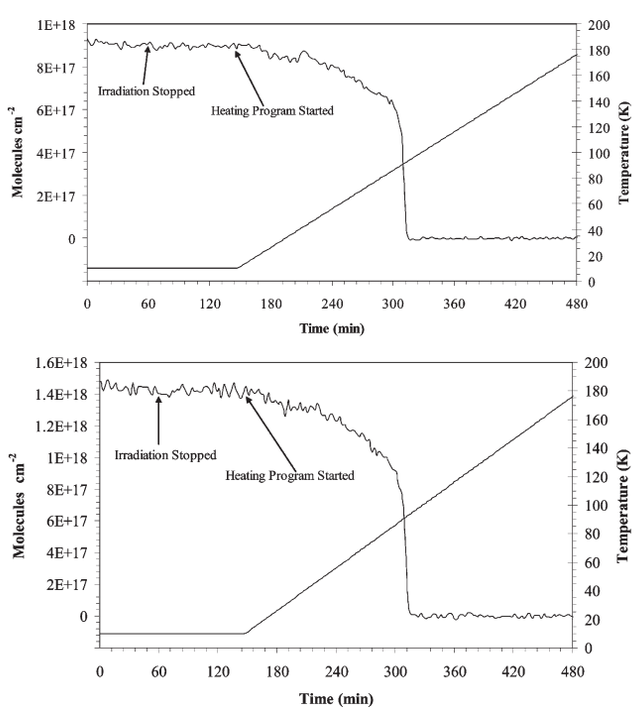

Fig. 8 Temporal development of the column densities of carbon dioxide molecules calculated *via* integrated absorptions at 3708 cm^{-1} (top) and 3600 cm^{-1} (bottom) during the experiment, the isothermal phase, and the heating period. The corresponding temperature profiles are overlaid.

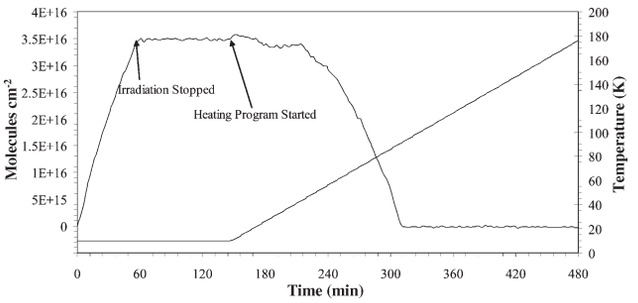

Fig. 9 Temporal development of the column densities of newly formed carbon monoxide molecules calculated *via* the integrated absorptions at 2139 cm^{-1} during the experiment, the isothermal phase, and the heating period. The corresponding temperature profile is overlaid.

clear that the observed carbon trioxide molecule has a cyclic, C_{2v} symmetric structure. Neither the C_s nor the D_{3h} symmetric structures of carbon trioxide were observed.

Besides the carbon monoxide and the carbon trioxide molecules, we were also able to identify the ozone molecule (Fig. 7). Two absorptions at 1042 cm^{-1} (ν_3, anti symmetric stretch) and the weaker bending mode at 704 cm^{-1} (ν_2) were identified. These data agree very well with previous assignments.[36]

4.2.2 Quantitative analysis. Figs. 8–11 compile the temporal development of the column densities of the carbon

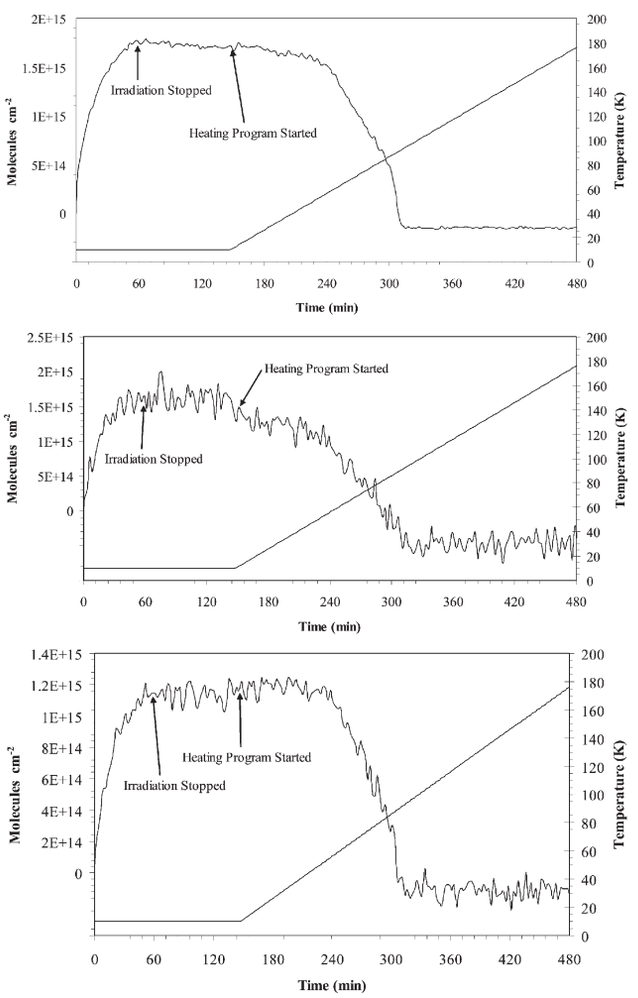

Fig. 10 Temporal development of the column densities of newly formed carbon trioxide molecules calculated *via* the integrated absorptions at 2044 cm^{-1} (top), 1067 cm^{-1} (center), and 972 cm^{-1} (bottom) during the experiment, the isothermal phase, and the heating period. The corresponding temperature profiles are overlaid.

This journal is © The Owner Societies 2004

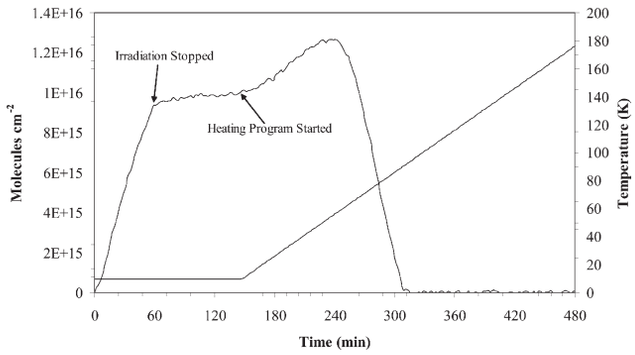

Fig. 11 Temporal development of the column densities of newly formed ozone molecules calculated *via* the integrated absorptions at 1042 cm^{-1} during the experiment, the isothermal phase, and the heating period. The corresponding temperature profile is overlaid.

dioxide reactant and of the products (carbon monoxide, carbon trioxide, and ozone) during the irradiation at 10 K, the consecutive equilibration period at 10 K, and the heating phase. During the irradiation of the carbon dioxide ice, the column density of the CO_2 molecules decreases only slightly from 1.188×10^{18} cm^{-2} to 1.158×10^{18} cm^{-2} (Fig. 8); note that these data are afflicted with an error of ±25% (Table 2). This means that only 3.01×10^{16} cm^{-2}, *i.e.* 2.5%, of the carbon dioxide molecules are destroyed at the end of the irradiation (Table 5). Accounting for the target surface and the electron beam current, we can conclude that each implanted electron destroys 17 ± 4 CO_2 cm^{-2}, *i.e.* 51 ± 13 carbon dioxide molecules. As expected, the carbon dioxide column density stays constant during the isothermal phase. With increasing temperature the CO_2 molecules sublime; as the temperature is raised from 10 K to 20 K, strengths of all carbon dioxide absorptions start to diminish; at 94 K, no solid carbon dioxide is left on the silver waver.

With decreasing carbon dioxide column density, new absorptions arise from carbon monoxide (Fig. 9) and carbon trioxide (Fig. 10). The carbon monoxide column density rises almost linearly with increasing irradiation time to $3.5 \pm 0.4 \times 10^{16}$ cm^{-2}, *i.e.* an average production rate of 60 ± 6 carbon monoxide molecules per implant, *i.e.* 20 ± 2 CO cm^{-2}; the integral absorption coefficient for the 2139 cm^{-1} band of 1.1×10^{-17} molecules cm^{-1} is accurate to ±10%. On the other hand, the carbon trioxide column density rises quickly but starts to saturate toward the end of the experiment at 1.8×10^{15} cm^{-2} (2044 cm^{-1}), 1.5×10^{15} cm^{-2} (1067 cm^{-1}), and 1.1×10^{15} cm^{-2} (972 cm^{-1}). These data translate to a synthesis of 2.5 ± 0.5 carbon trioxide molecules per electron (0.8 ± 0.2 CO_3 cm^{-2} per electron; production rates are averaged over those obtained from three CO_3 fundamentals).

Based on these information, we can now investigate the carbon balance of the target. Based on our integration routine, $3.0 \pm 0.8 \times 10^{16}$ CO_2 cm^{-2} lead to the formation of $3.5 \pm 0.4 \times 10^{16}$ CO cm^{-2} and $1.5 \pm 0.3 \times 10^{15}$ CO_3 cm^{-2}, *i.e.* destruction of $3.0 \pm 0.8 \times 10^{16}$ cm^{-2} *versus* formation of $3.7 \pm 0.4 \times 10^{16}$ cm^{-2}; within the error limits, we can conclude that the carbon budget is conserved in the experiment. This strongly correlates with our experimental findings that carbon dioxide and carbon trioxide are the only newly formed carbon-bearing species in our experiment. Note that whereas the carbon monoxide column density stays constant during the isothermal phase at 10 K, the carbon trioxide column density seems to decrease slightly by 5%. However, since the integration is accurate only to 10%, the drop of the 2044 cm^{-1} absorption might be within the experimental error limits: similar the increasing carbon monoxide column density upon warming the matrix to 20 K; alternatively we might conclude that the carbon trioxide molecule starts to decompose even at 10 K. Upon heating the target, both the carbon monoxide and carbon trioxide column

Table 4 New infrared absorptions of the processed carbon dioxide sample at 10 K

Observed frequency/cm^{-1}	Species	Assignment
2045	CO_3	ν_1 (C=O stretch)
1879	CO_3	Fermi resonance
1068	CO_3	ν_2 (O–O stretch)
973	CO_3	ν_5 (C–O stretch)
565	CO_3	ν_6 (O–C=O stretch)
2139	CO	ν_1 (CO stretching)
2092	^{13}CO	ν_1 (^{13}CO stretching)
1042	O_3	ν_3 (anti symmetric stretch)
704	O_3	ν_2 (bending mode)

Table 5 Destruction (CO_2) and formation (CO, CO_3, O_3) of molecules after the 10 K irradiation phase; data for ozone are also give at 10 K. Units are given in column densities (n/molecule cm^{-2}), in molecules synthesized per electron per cm (n'), and molecules synthesized per electron (n'')

Molecule	n/molecule cm^{-2}	n'/molecule electron^{-1} cm^{-2}	n''/molecule electron^{-1}
CO_2	$-3.0 \pm 0.8 \times 10^{16}$	-17 ± 4	-51 ± 13
CO	$3.5 \pm 0.4 \times 10^{16}$	20 ± 2	60 ± 6
CO_3	$1.5 \pm 0.3 \times 10^{15}$	0.8 ± 0.2	2.5 ± 0.5
O_3 (10 K)	$9.3 \pm 1.3 \times 10^{15}$	5 ± 1	15 ± 3
O_3 (60 K)	$1.3 \pm 0.2 \times 10^{16}$	7 ± 1	21 ± 3
ΔO_3	$3.7 \pm 1.0 \times 10^{15}$	2 ± 1	6 ± 3

Table 6 Integral absorption coefficients A used in this work. The fundamentals of the carbon trioxide isomer are compiled in Table 3

Molecule	Absorption/cm^{-1}	A/cm molecule^{-1}
CO	2139	1.1×10^{-17}
O_3	1042	1.4×10^{-17}
O_3	704[b]	5.5×10^{-19}
CO_2	3708	1.4×10^{-18}
CO_2	3600	4.5×10^{-19}
CO_3	1879[a]	3.1×10^{-17}

[a] The 2045 cm^{-1} absorption has an integrated area of 0.529 cm^{-1} and $A = 8.9 \times 10^{-17}$ cm molecule^{-1}. Considering an area of the 1879 cm^{-1} band of 0.18 cm^{-1}, the integral absorption coefficient of the 1879 cm^{-1} absorption calculates to 3.1×10^{-17} cm molecule^{-1}. [b] The 1042 cm^{-1} absorption has an integrated area of 0.440 cm^{-1} and $A = 1.4 \times 10^{-17}$ cm molecule^{-1}. Considering an area of the 704 cm^{-1} band of 0.018 cm^{-1}, the integral absorption coefficient of the 704 cm^{-1} absorption calculates to 5.5×10^{-19} cm molecule^{-1}.

Table 7 Calculated equilibrium constants K for the isomerization of **s2** ↔ **s1**

Temperature/K	Equilibrium constant K
10	0.002176482
20	0.026952237
30	0.062358629
40	0.094845045
50	0.121988944
60	0.144277400
70	0.162660463
80	0.178018439
90	0.191041466

densities decrease. Note, however, that whereas the carbon dioxide absorptions disappear at 94 K, no carbon monoxide and carbon trioxide bands were observed at temperatures higher than 91 K. At 91 K, a column density of $5.6 \pm 1.2 \times 10^{17}$ CO_2 cm^{-2} remains (0.21 ± 0.04 μm CO_2 ice). Since the carbon dioxide matrix sublimes in layers, those layers exposed to the vacuum sublime first. Considering an initial column density of 1.188×10^{18} cm^{-2} CO_2 cm^{-2} (0.48 ± 0.11 μm CO_2 ice), we can conclude that the newly synthesized molecules are formed within the first 0.28 ± 0.09 μm of the sample, *i.e.* those layers which are subliming first into the vacuum. Once these layers have been released, the remaining carbon dioxide ice of 0.20 ± 0.04 μm does not contain any newly formed molecules. This in turn indicates that the 5 keV electrons are absorbed and induce radiation damage within the first 0.28 ± 0.09 μm of the carbon dioxide sample.

Compared to the carbon oxides, the temporal development of ozone depicts striking differences (Fig. 11). The ozone column density increases after 60 min irradiation time to $9.3 \pm 1.3 \times 10^{15}$ cm^{-2}; data has been calculated with an integral absorption coefficient of $1.4 \pm 0.2 \times 10^{-17}$ molecules cm^{-1}. This requires a destruction of $2.8 \pm 0.4 \times 10^{16}$ CO_2 cm^{-2}. Statistically, each electron generates 15 ± 3 O_3 molecules in the sample. Since the formation of a single ozone molecule requires the destruction of three carbon dioxide molecules to initiate three oxygen atoms, 45 ± 9 carbon dioxide molecules have to be destroyed to account for the experimentally derived ozone production rate. To account for the total oxygen balance after the irradiation, we have to include the newly synthesized carbon trioxide molecules ($1.5 \pm 0.3 \times 10^{15}$ cm^{-2}), too. Hence, the total oxygen column density of the freshly formed molecules calculates as the sum of the carbon trioxide column density plus three times the ozone column density; based on these considerations, a column density of $2.9 \pm 0.4 \times 10^{16}$ cm^{-2} has to be generated in the carbon dioxide ice by the electrons. On the other hand, the decay profile of the carbon dioxide absorptions suggest that $3.0 \pm 0.8 \times 10^{16}$ CO_2 cm^{-2} have been destroyed after the irradiation. Since each carbon dioxide molecule fragments to carbon monoxide and atomic oxygen upon interaction with an electron, we would expect an identical number of oxygen atoms to be incorporated inside the newly formed molecules, *i.e.* ozone and carbon trioxide. Within the error limits, the oxygen balance seems to hold.

During the isothermal phase, the ozone column density slightly increases from $9.3 \pm 1.3 \times 10^{15}$ cm^{-2} to $1.0 \pm 0.1 \times 10^{16}$ cm^{-2} during the 10 K equilibration period; this suggest that oxygen atoms, which are mobile at 10 K, are present in the carbon dioxide matrix and may react with molecular oxygen to form additional ozone. We have to keep in mind that this analysis only comprises the oxygen balance of the infrared active molecules, but not of infrared inactive species such as molecular and atomic oxygen. In the solid state, the O_2 absorptions at 1591 cm^{-1} and 1617 cm^{-1} hold absorption coefficients of about 10^{-21} cm $molecule^{-1}$ (ref. 37). It is not surprising that we were unable to detect these transitions in our experiments. Therefore, we can conclude that molecular oxygen and oxygen atoms reside inside the carbon dioxide matrix as well. This effect is even more pronounced while the sample is heated to 60 K. Here, the ozone column density rises significantly by about 30% reaching a maximum at $1.3 \pm 0.2 \times 10^{16}$ cm^{-2} before the column density drops sharply due to the subliming carbon dioxide matrix. This suggests that at least $1.1 \pm 0.3 \times 10^{16}$ cm^{-2} of the oxygen atoms exist in the form of molecular or atomic oxygen. Including the enhanced ozone column density in the oxygen balance gives a column density of generated oxygen atoms of $4.0 \pm 0.6 \times 10^{16}$ cm^{-2} *versus* destruction of the carbon dioxide molecules of $3.0 \pm 0.8 \times 10^{16}$ cm^{-2}. At 92 K, the ozone absorption disappears completely. It is interesting to compare this temperature with those where the bands of carbon monoxide 91 K, carbon trioxide 91 K, and carbon dioxide 94 K vanish. As indicated in the previous section, carbon monoxide, carbon trioxide, and the oxygen atoms are formed initially in the first 0.28 ± 0.09 μm of the carbon dioxide sample. As the temperature rises, oxygen atoms diffuse and could penetrate also those regions of the carbon dioxide ice which has not been penetrated by the electrons; here, the oxygen atoms could recombine to ozone. This could explain the presence of ozone absorptions at the temperature of 92 K where absorptions of carbon monoxide and carbon trioxide are absent due to their sublimation with the outer layers of the carbon dioxide matrix into the vacuum.

4.3 Mass spectrometry

It is interesting to correlate the infrared observations with a mass spectrometric analysis of the gas phase. During the annealing phase of the sample, the carbon dioxide matrix and the newly formed molecules (CO_3, CO, O_3) sublime into the gas phase. Upon heating the sample to 25 K (180 min experimental time), the carbon dioxide matrix start to sublime (Fig. 8); similarly, the embedded carbon monoxide molecules are being released into the gas phase (Fig. 9). Note that the ozone column density increases upon warming the sample due to reactions of atomic oxygen with molecular oxygen (section 4.2); at 60 K (240 min experimental time), the ozone column density decreases, too. However, the mass spectrometric results do not correlate entirely with the infrared data. Although the partial pressure of carbon monoxide begins to increase at 25 K (as expected from the infrared data), the temporal development of the partial pressure of ozone shows two distinct peaks: a small hump starting at 240 min experimental time (60 K), and a second intense peak at 291 min experimental time (Fig. 12). A similar pattern has been observed for the carbon dioxide molecule, too. To interpret the discrepancy between the infrared and mass spectrometric data, we have to keep in mind that the silver target (first stage) is annealed while the cold head is still in operation; this means that the outer aluminum cold shield, which is mounted to the second stage of the closed cycle helium refrigerator, is still cooled down. Therefore, the molecules subliming during the annealing phase of the silver target (first ozone peak) can actually re-condense onto the aluminum cold shield. Once the heat load from the cartridge heater increase also the temperature of the second cold head stage, those molecules condensed on the aluminum shield can sublime, too (second ozone peak). Note that two peaks were observed only for ozone, carbon dioxide, and oxygen, but not for carbon monoxide. Here, carbon monoxide does not re-condense at the 50 K aluminum cold

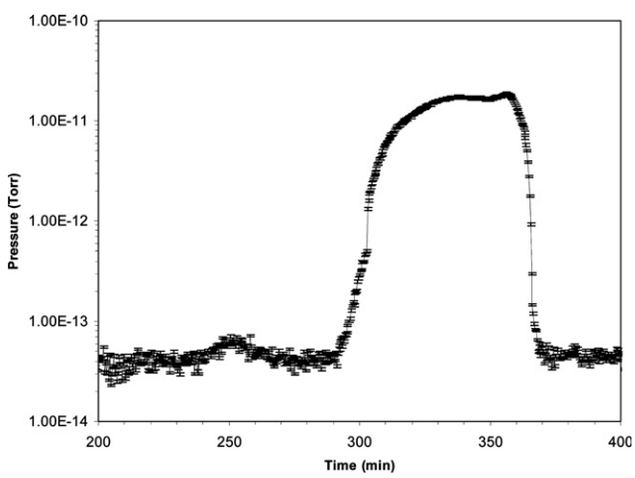

Fig. 12 Temporal development of the ozone partial pressure and corresponding error bars as extracted from the mass spectrometric data *via* matrix interval algebra.

 This journal is © The Owner Societies 2004

shield since carbon monoxide ice is unstable at temperatures higher than 30 K.

5 Discussion

Our investigations indicate that the response of the carbon dioxide system upon the keV electron bombardment is governed by an initial formation of carbon monoxide and atomic oxygen, eqns. (3)–(4). Depending on the energy transfer form the impinging electron to the carbon dioxide molecule, the oxygen atom can be generated either in its electronic ground (^{3}P) *via* inter system crossing to the triplet manifold and/or excited state (^{1}D) on the singlet surface.

$$CO_2(X\ ^1\Sigma_g^+) \rightarrow CO(X\ ^1\Sigma^+) + O(^3P), \quad (3)$$

$$CO_2(X\ ^1\Sigma_g^+) \rightarrow CO(X\ ^1\Sigma^+) + O(^1D). \quad (4)$$

These reactions are endoergic by 532 kJ mol^{-1} (5.51 eV) and 732 kJ mol^{-1} (7.59 eV), respectively. Our experiments indicate that each electron initiates 60 ± 6 CO molecules within the carbon dioxide ice (Table 5); this translates to 331 ± 33 eV and 455 ± 46 eV to form O(^{3}P) and O(^{1}D), respectively. Considering the energy of the electron of 5 keV, about 10% of its kinetic energy is utilized to cleave the carbon–oxygen bonds of the carbon dioxide molecules; note that this calculation assumes all the carbon monoxide molecules are formed in their vibrational ground states; also, the oxygen atoms have no excess translational energy. However, to escape the matrix cage, the oxygen atom must have at least 0.5 eV excess kinetic energy; if its kinetic energy is less than the lattice bonding energy, at least O(^{1}D) can react back without an entrance barrier to recycle the carbon dioxide molecule. To fit the experimentally obtained profile of the carbon dioxide and carbon monoxide column densities, we employed the following model. The carbon monoxide molecule was assumed to 'decay' first order upon electron bombardment similar to a radioactive decay, *i.e.* it follows the velocity law (5) (the square brackets indicate the column density in cm^{-2}; $I_e = 4.92 \times 10^{11}$ s^{-1} presents the electron current in electrons s^{-1}):

$$-d[CO_2]/dt = k_1 I_e[CO_2] = k_1'[CO_2], \quad (5)$$

$$d[CO]/dt = k_2 I_e[CO_2] = k_2'[CO_2]. \quad (6)$$

This translates to the following temporal evolutions of the column density for carbon dioxide (7) and carbon monoxide (8) with the constant a:

$$[CO_2](t) = [CO_2](t=0)e^{k_1' t}, \quad (7)$$

$$[CO](t) = a(1 - e^{-k_2' t}). \quad (8)$$

The best fits of the carbon dioxide and carbon monoxide profiles are shown in Figs. 13 and 14, respectively, with $[CO_2](t=0) = 1.19 \pm 0.30 \times 10^{18}$ cm^{-2}, $k_1' = 7.35 \pm 0.20 \times 10^{-6}$ s^{-1}, $a = 7.1 \pm 0.7 \times 10^{16}$ cm^{-2}, and $k_2' = 1.93 \pm 0.1 \times 10^{-4}$ s^{-1}. Accounting for the electron current, this yields $k_1 = 1.5 \pm 0.2 \times 10^{-17}$ and $k_2 = 3.9 \pm 0.2 \times 10^{-16}$.

We now investigate the fate of the generated oxygen atoms quantitatively. Our data indicate that the carbon trioxide molecule is formed *via* reaction of atomic oxygen with carbon dioxide. We were able to fit the temporal development of the column density assuming that a carbon dioxide dimer decomposed to carbon dioxide, atomic oxygen, and carbon monoxide; within the matrix cage, the generated oxygen atom reacts with the non-reacted carbon dioxide to form carbon trioxide *via* eqns. (9) and (10):

$$-d[(CO_2)_2]/dt = k_3 I_e[(CO_2)_2] = k_3'[(CO_2)_2], \quad (9)$$

$$d[CO]/dt = k_4 I_e[(CO_2)_2] = k_4'[(CO_2)_2]. \quad (10)$$

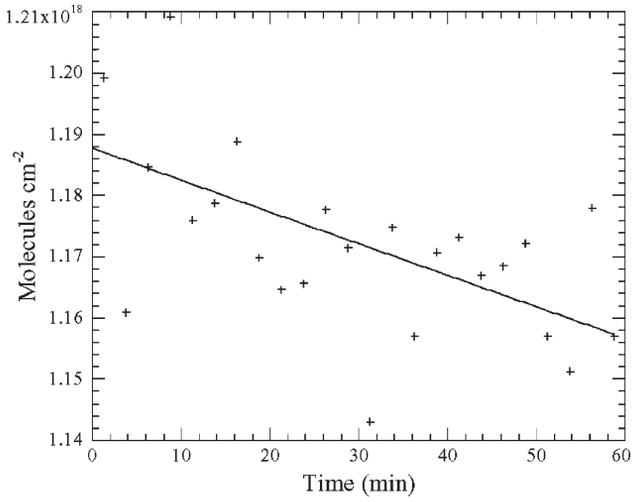

Fig. 13 Exponential fit of the carbon dioxide column density according to eqn. (7). Error bars of the data are ±10%.

This leads to the temporal evolution of the column density for carbon trioxide *via* eqn. (11):

$$[CO_3](t) = b(1 - e^{-k_4' t}). \quad (11)$$

Fig. 15 depicts the best fit of the carbon trioxide profile respectively, with $b = 1.5 \pm 0.3 \times 10^{15}$ cm^{-2}, and $k_4' = 1.1 \pm 0.1 \times 10^{-3}$ s^{-1}. Accounting for the electron current, this yields $k_4 = 2.2 \pm 0.2 \times 10^{-15}$. Extrapolating eqns. (8) and (11) for $t \rightarrow \infty$ and extracting the ratio of $[CO](t=\infty)/[CO_3](t=\infty)$ calculates the fraction of released oxygen atoms reacting with carbon dioxide to 47 ± 14. This means that only 2.1 ± 0.5% of the generated oxygen atoms react to carbon trioxide.

What might be the reason for the low fraction of oxygen atoms reacting to carbon dioxide? The potential energy surface (Fig. 4) helps to understand this scenario. First, the experiments clearly indicated the formation of the cyclic **s1** isomer; neither **s2** nor **t2** have been detected. Our calculations show that in the gas phase, only the addition of O(^{1}D) can form **s1** *via* **s5** and **s-TS3**. This is a clear indication that the interaction of energetic electrons with the carbon dioxide molecules generates reactive oxygen atoms. However, this reaction has to pass **s-TS3** which is located 5.6–7.6 kJ mol^{-1} above the separated reactants. This requires that the O(^{1}D) reactant has at least 5.6–7.6 kJ mol^{-1} excess kinetic energy to overcome the barrier. Once **s1** has been formed in the solid state, the

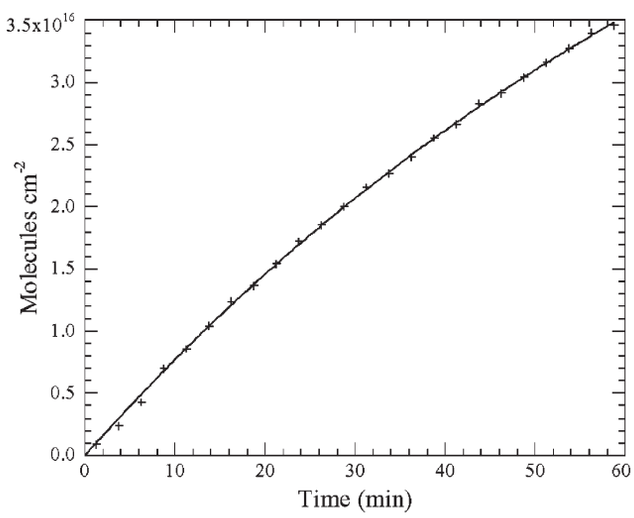

Fig. 14 Exponential fit of the carbon monoxide column density according to eqn. (8). Error bars of the data are ±10%.

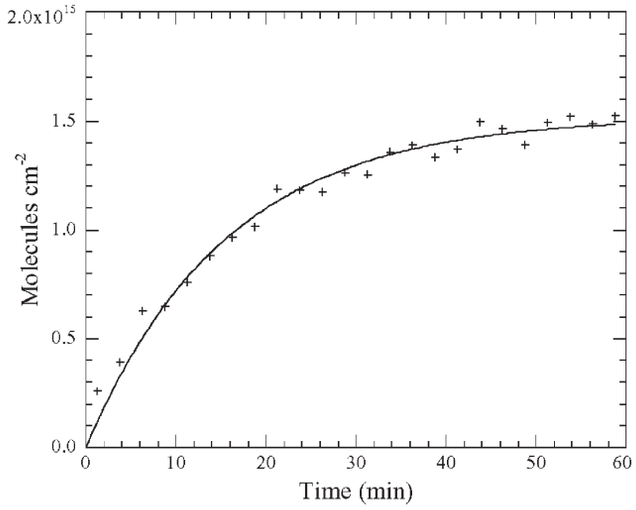

Fig. 15 Exponential fit of the carbon trioxide column density according to eqn. (11). Error bars of the data are ±20%.

surrounding matrix can divert the internal energy (197.5 kJ mol^{-1}) of the carbon trioxide species; this stabilizes the latter and prevents an isomerization *via* **s-TS1** to **s2**. Non-reactive $O(^1D)$ can be quenched in the matrix easily *via* intersystem crossing to the ^3P ground state.[38] On the triplet surface, ground state oxygen atoms can react solely to yield **t1**; followed by intersystem crossing, the latter can form **s2** in the carbon dioxide matrix. However, since only the cyclic carbon trioxide isomer was detected, this pathway can be likely ruled out. Similarly, the electronically excited $^1A''$ surface can be excluded to contribute to the formation of the cyclic carbon trioxide isomer since only **s4** can be formed *via* **s3** and **s-TS2**. Instead, we located the seam of crossing (MSX) which connects the triplet to the singlet surface. In the gas phase, this crossing is located close to **t-TS1**, and $O(^3P)$ with a sufficient amount of kinetic energy can surpass this barrier to form also **s1**. In the solid matrix, however, the energy of MSX is likely lowered; the exact barrier height is currently under investigation. Actually, the calculated equilibrium constants for the isomerization **s2** ↔ **s1** correlate with the failed observation of the D_{3h} symmetric CO_3 isomer in the ice matrix. Here, $K(10\ K) = 0.002176482$ means that at 10 K the concentration of **s1** should be 500 times higher than that of **s2**, if they are in equilibrium. The spectroscopic data suggest that the remaining oxygen atoms rather react *via* molecular oxygen to form ozone *via* eqns. (12)–(13). Note that only ground state reactants have been considered; this is certainly true for the reaction during the equilibrating phase at 10 K and the annealing program to 60 K. However, during the electron bombardment, $O(^1D)$ atoms could react, too. Both reactions are exoergic by 498.5 kJ mol^{-1} and 106.5 kJ mol^{-1}, respectively and involve no entrance barrier except the diffusion energy of the oxygen atoms to migrate to the reaction site. The ability of the oxygen atoms to diffuse even at 10 K and in particular at elevated temperatures has been established previously (section 4.2. and Fig. 11). The detailed formation mechanism of ozone *via* eqn. (13) and/or electronically excited species is currently under investigation and might involve a short-lived cyclic ozone molecule. So far, we were not able to fit the temporal evolution of the ozone column density; this fit requires knowledge of the diffusion coefficient of the oxygen atom which is currently under study. A simple exponential fit fails as expected since the ozone is clearly a higher-order reaction product.

$$O(^3P) + O(^3P) \rightarrow O_2(X\ ^3\Sigma_g^-), \qquad (12)$$

$$O_2(X\ ^3\Sigma_g^-) + O(^3P) \rightarrow O_3(X\ ^1A_1). \qquad (13)$$

Finally, we would like to comment on the possibility to generate reactive carbon atoms *via* the interaction of energetic electrons with carbon dioxide. Recall that the slight increase of the carbon monoxide column density in the equilibration phase (Fig. 9) could indicate a recombination of diffusive carbon atoms with mobile oxygen atoms, eqn. (14), a process similar to the formation of molecular oxygen according to eqn. (12).

$$C(^3P) + O(^3P) \rightarrow CO(X\ ^1\Sigma^+). \qquad (14)$$

Detailed electronic structure calculations depicted that a release of carbon atoms from a linear carbon dioxide molecule does not occur.[39] Instead, the linear carbon dioxide species has to isomerize first to a cyclic structure which lies 582 kJ mol^{-1} higher in energy than the linear structure. The cyclic isomer ring opens and forms a linear $COO(X\ ^1\Sigma^+)$ molecule which then loses a carbon atom in its excited ^1D state. However, our experiments identify neither the cyclic carbon dioxide nor the linear $COO(X\ ^1\Sigma^+)$ molecule as a reactive intermediate in our matrix. Since the carbon budget is conserved in our experiment (section 4.2.2) we suggest that the contribution of reactive carbon atoms, if any, is only minor.

6 Astrophysical and planetary implications

Carbon dioxide ice presents also a major constituent of ices as condensed on sub-micrometre sized grain particles in cold interstellar clouds. Although the dust component embodies only 1% of the interstellar matter, these nuclei play a key role in the formation of new molecules. Deep in the interior of dense clouds, grain particles effectively shield newly synthesized molecules in the gas phase from the destructive external UV radiation field. Most important, these sub micrometer sized particles present valuable nurseries to synthesize new molecules. In dense clouds, these grains have typical temperatures of 10 K.[40,41] Once molecules, radicals, or atoms from the gas phase collide with the solid particle, they are accreted on the grain surface resulting in an icy mantle up to 0.1 μm thick. At ultralow temperatures, all species except H, H_2, and He hold sticking coefficients of unity. This means that each collision of a gas phase species with a cold surface leads to an absorption and hence thickening of the ice layer. Here, solid mixtures containing H_2O (100), CO (7–27), CH_3OH (<3.4), NH_3 (<6), CH_4 (<2), and CO_2 (15) were identified unambiguously *via* infrared spectroscopy towards the dense cloud TMC-1 employing the field star Elias 16 as a black body source;[42] the numbers in parentheses indicate the relative abundances compared to water ice.

These molecular clouds are interspersed with ultraviolet photons (<13.2 eV) and energetic particles from T-Tauri winds, stellar jets, carbon stars, and galactic cosmic ray particles. Therefore, pristine ice mantles are processed chemically by the cosmic ray induced internal ultraviolet radiation present even in the deep interior of dense clouds ($\phi = 10^3$ photons $cm^{-2}\ s^{-1}$) and in particular through particles of the galactic cosmic radiation field. This can lead to the formation of new molecules in the solid state *via* non-equilibrium (non-thermal) chemistry even at temperatures as low as 10 K. The particle component of the cosmic ray radiation field consists of 97–98% protons (p, H^+) and 2–3% helium nuclei (α-particles, He^{2+}) in the low energy range of 1–10 MeV (1 MeV = 10^6 eV) with $\phi = 10$ particles $cm^{-2}\ s^{-1}$.[43] It has been well established that cosmic ray MeV particles penetrate the ice mantles and the grain core and deposit parts of their energy inside the ices *via* interaction of the MeV implant and the electronic system of the ice molecules.[44] Detailed dynamics simulation showed that 99.9% of the transferred energy leads predominantly to ionization and hence release of energetic (keV)

This journal is © The Owner Societies 2004

electrons perpendicularly to the trajectory of the MeV implant (ultra track). Therefore, our experiments simulate also the energetic processes in the ultra track of MeV particles inside interstellar and also cometary ices. Based on these considerations, we can conclude that the cyclic carbon trioxide molecule should also be present in carbon-dioxide-rich extraterrestrial ices which have been identified in interstellar clouds, comets, and also on Mars. Most importantly, our experiments indicated the initial formation of suprathermal (electronically excited) oxygen atoms. In extraterrestrial ices, the species do not react solely with the carbon dioxide ice, but with the remaining ice components. In particular the $O(^1D)$ atoms are very reactive and may destroy newly formed, astrobiologically important molecules such as sugars and amino acids even deep inside ices. Potential organics inside the Martian soil might be degraded easily by energetic oxygen atoms. Also, the interaction of carbon dioxide ices on Mars (and in comets as well as in the interstellar medium) with MeV particles produces significant amounts of ozone. Upon warming the ices, molecules would sublime and could contribute considerably to the ozone budget in the Martian atmosphere.

Our investigations help to understand a potential ^{18}O enrichment in the terrestrial and Martian atmospheres. Whereas the cyclic carbon trioxide isomer is being stabilized upon reaction of electronically excited oxygen atoms with carbon dioxide in the matrix *via* phonon interaction, in the gas phase the cyclic carbon trioxide molecule can isomerizes to the D_{3h} isomer. This could scramble the incorporated ^{18}O and hence lead to an enrichment of ^{18}O within the carbon dioxide once the carbon trioxide molecule decomposes too atomic oxygen and carbon dioxide (Fig. 16).

7 Conclusions

We investigated the synthetic routes to form the cyclic carbon trioxide isomer, $CO_3(X\ ^1A_1)$, in carbon-dioxide-rich extraterrestrial ices and in the atmospheres of Earth and Mars experimentally and theoretically. The studies indicate that the interaction of an electron with a carbon dioxide molecule is dictated by a carbon–oxygen bond cleavage to form ground state (^3P) and/or electronically excited (^1D) oxygen atoms plus a carbon monoxide molecule. About 2% of the oxygen atoms react with carbon dioxide molecules to form the C_{2v} symmetric, cyclic CO_3 structure, *via* addition to the carbon–oxygen double bond of the carbon dioxide species; neither the C_s nor the D_{3h} symmetric isomers of carbon trioxide were detected. Since the addition of $O(^1D)$ involves a barrier of 5.6–7.6 kJ mol^{-1} and the reaction of $O(^3P)$ with carbon dioxide to form the carbon trioxide molecule *via* triplet-singlet intersystem crossing is endoergic by 2 kJ mol^{-1}, the atomic oxygen reactant(s) must have also access kinetic energy. The remaining oxygen atoms react barrier-less to form ozone *via* molecular oxygen. In our matrix, $CO_3(X\ ^1A_1)$ is being stabilized by phonon interactions to the surrounding matrix. In the gas phase, however, the initially formed C_{2v} structure can ring-open to the D_{3h} isomer which in turn loses an oxygen atom to 'recycle' carbon dioxide. The atomic oxygen exchange pathway has been confirmed in a recent crossed molecular beams experiment; however, the authors were not able to assign the nature if the CO_3 intermediate explicitly.[45] This process could contribute significantly to an ^{18}O enrichment in carbon dioxide in the atmospheres of Earth and Mars.

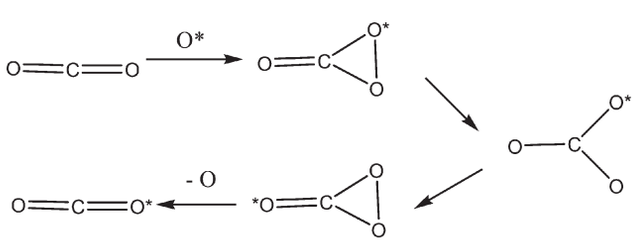

Fig. 16 Schematic mechanism for potential enrichment of ^{18}O (O*) in carbon dioxide.

Acknowledgements

This project has been supported by The University of Hawai'i (USA) (CJB, CJ, RIK), Osaka Vacuum Ltd. (Japan), the Particle Physics and Astronomy Research Council (PPARC, UK) (RIK), and Florida International University (AMM).

References

1 N. G. Moll, D. R. Clutter and W. E. Thompson, *J. Chem. Phys.*, 1966, **45**, 4469.
2 M. E. Jacox and D. E. Milligan, *J. Chem. Phys.*, 1971, **54**, 919.
3 E. Weissberger, W. H. Breckenridge and H. Taube, *J. Chem. Phys.*, 1967, **47**, 1764.
4 P. LaBonville, R. Kugel and J. R. Ferraro, *J. Chem. Phys.*, 1977, **67**, 1477.
5 Y. L. Yung and W. B. DeMore, *Photochemistry of Planetary Atmospheres*, Oxford University Press, Oxford, 1999.
6 D. D. Bogard, R. N. Clayton, K. Marti, T. Owen and G. Turner, *Space Sci. Rev.*, 2001, **96**(1–4), 425.
7 V. I. Moroz, *Adv. Space Res.*, 1998, **22**(3), 449.
8 E. M. Galimov, *Dokl. Akad. Nauk*, 1997, **355**(3), 382.
9 S. K. Atreya and Z. G. Gu, *Adv. Space Res.*, 1995, **16**(6), 57.
10 A. A. Fedorova *et al.*, *Planet. Space Sci.*, 2002, **50**, 3.
11 M. H. Thiemens, T. L. Jackson and C. A. M. Brenninkmeijer, *Geophys. Res. Lett.*, 1995, **22**(3), 255.
12 J. Wen and M. H. Thiemens, *J. Geophys. Res.*, 1993, **98**, 12 801.
13 Y. L. Yung and A. Y. T. Lee *et al.*, *J. Geophys. Res.*, 1997, **102**, 10 857.
14 B. Lutz *et al.*, *Nature*, 1999, **400**, 547.
15 P. H. Wine and A. R. Ravishankara, *Chem. Phys. Lett.*, 1981, **77**, 103.
16 R. A. Young, G. Black and T. G. Slanger, *J. Chem. Phys.*, 1968, **49**, 4758.
17 http://kinetics.nist.gov/index.php.
18 W. Tsang and R. F. Hampson, *J. Phys. Chem. Ref. Data*, 1986, **15**, 1087.
19 R. D. J. Froese and J. D. Goddard, *J. Phys. Chem.*, 1993, **97**, 7484.
20 A. S. Averyanov, Y. G. Khait and Y. V. Puzanov, *J. Mol. Struct.*, 1999, **459**, 95.
21 A. B. Ivanov and D. O. Muhleman, *Icarus*, 2001, **154**(1), 190.
22 A. Colaprete and O. B. Toon, *J. Geophys. Res., [Planets]*, 2002, **107**(E7), 5/1.
23 R. T. Clancy and B. J. Sandor, *Geophys. Res. Lett.*, 1998, **25**(4), 489.
24 H. J. Fraser, M. R. S. McCoustra and D. A. Williams, *Astron. Geophys.*, 2002, **43**, 10.
25 P. Ehrenfreud and W. A. Schutte, in: *Astrochemistry – From Molecular Clouds to Planetary Systems*, ASP Publishing, San Francisco, 2000.
26 H.-J. Werner and P. J. Knowles, *J. Chem. Phys.*, 1985, **82**, 5053.
27 P. J. Knowles and H.-J. Werner, *Chem. Phys. Lett.*, 1985, **115**, 259.
28 H.-J. Werner and P. J. Knowles, *J. Chem. Phys.*, 1988, **89**, 5803.
29 P.-J. Knowles and H.-J. Werner, *Chem. Phys. Lett.*, 1988, **145**, 514.
30 R. D. Amos, A. Bernhardsson, A. Berning, P. Celani, D. L. Cooper, M. J. O. Deegan, A. J. Dobbyn, F. Eckert, C. Hampel, G. Hetzer, P. J. Knowles, T. Korona, R. Lindh, A. W. Lloyd, S. J. McNicholas, F. R. Manby, W. Meyer, M. E. Mura, A. Nicklass, P. Palmieri, R. Pitzer, G. Rauhut, M. Schütz, U. Schumann, H. Stoll, A. J. Stone, R. Tarroni, T. Thorsteinsson and H.-J. Werner, *MOLPRO, a package of ab initio programs designed by H.-J. Werner and P. J. Knowles, Version 2002.1*, 2002.
31 T. Helgaker, H. J. Aa. Jensen, P. Jørgensen, J. Olsen, K. Ruud, H. Ågren, A. A. Auer, K. L. Bak, V. Bakken, O. Christiansen, S. Coriani, P. Dahle, E. K. Dalskov, T. Enevoldsen, B. Fernandez, C. Hättig, K. Hald, A. Halkier, H. Heiberg, H. Hettema, D. Jonsson, S. Kirpekar, R. Kobayashi, H. Koch,

K. V. Mikkelsen, P. Norman, M. J. Packer, T. B. Pedersen, T. A. Ruden, A. Sanchez, T. Saue, S. P. A. Sauer, B. Schimmelpfennig, K. O. Sylvester-Hvid, P. R. Taylor and O. Vahtras, *DALTON, a molecular electronic structure program, Release 1.2*, 2001.
32 *Ices in the Solar System – Proceedings of the NATO advanced Research Workshop*, ed. J. Klinger, D. Benest, A. Dollfus and R. Smoluchowski, D. Reidel, Dordrecht, 1985.
33 R. I. Kaiser, P. Jansen, K. Petersen and K. Roessler, *Rev. Sci. Instrum.*, 1995, **66**(11), 5226.
34 R. I. Kaiser, A. Gabrysch and K. Roessler, *Rev. Sci. Instrum.*, 1995, **66**(4), 3059.
35 S. A. Sandford, L. J. Allamandola, A. G. G. M. Tielens and G. J. Valero, *Astrophys. J.*, 1988, **329**, 498.
36 T. Shimanouchi, *J. Phys. Chem. Ref. Data*, 1972, **6**(3), 993.
37 B. R. Cairns and G. C. Pimental, *J. Chem. Phys.*, 1965, **43**, 3432.
38 H.-J. Himmel, A. J. Downs and T. M. Greene, *Chem. Rev.*, 2002, **102**, 4191.
39 D.-Y. Hwang and A. M. Mebel, *J. Chem. Phys.*, 2000, **256**, 169.
40 D. C. B. Whittet, *Dust in the Galactic Environments*, Institute of Physics, Bristol, 1992.
41 A. G. G. M. Tielens and L. J. Allamandola, in: *Interstellar Processes*, eds., D. J. Hollenach and H. A. Thronson, Reidel, Dordrecht, 1987, 397.
42 B. Schmitt, in: *Molecules and Grains in Space*, ed. I. Nenner, American Institute of Physics, New York, 1994, 735.
43 R. I. Kaiser, G. Eich, A. Gabrysch and K. Roessler, *Astrophys. J.*, 1997, **484**, 487.
44 R. I. Kaiser and K. Roessler, *Astrophys. J.*, 1998, **503**, 959.
45 M. J. Perri, A. L. Van Wyngarden, K. A. Boering, J. J. Lin and Y. T. Lee, *J. Chem. Phys.*, 2003, **119**(16), 8213.
46 S. A. Sandford and L. J. Allamandola, *Astrophys. J.*, 1990, **355**, 357.
47 P. A. Gerakines, W. A. Schutte, J. M. Greenberg and E. F. van Dishoeck, *Astron. Astrophys.*, 1995, **296**, 810.

 This journal is © The Owner Societies 2004